# Terahertz referenceless wavefront sensing by means of computational shear-interferometry

MOSTAFA AGOUR,[1,2,*] CLAAS FALLDORF,[1] FATIMA TALEB,[3] ENRIQUE CASTRO-CAMUS,[3] MARTIN KOCH [3] AND RALF. B. BERGMANN[1,4]

[1]*BIAS - Bremer Institut für angewandte Strahltechnik GmbH, Klagenfurter Str. 5, 28359 Bremen, Germany*
[2]*Aswan University, Faculty of Science, Department of Physics, 81528 Aswan, Egypt*
[3]*Faculty of Physics and Material Sciences Center, Philipps-Universitat Marburg, Renthof 5, 35032 Marburg, Germany*
[4]*University of Bremen, Faculty 01: Physics and Electrical Engineering and MAPEX Center for Materials and Processes, 28359 Bremen, Germany*
[*]*agour@bias.de*

**Abstract:** In this contribution, we demonstrate the first referenceless measurement of a THz wavefront by means of shear-interferometry. The technique makes use of a transmissive Ronchi phase grating to generate the shear. We fabricated the grating by mechanical machining of high-density polyethylene. At the camera plane, the +1 and −1 diffraction orders are coherently superimposed, generating an interferogram. We can adjust the shear by selecting the period of the grating and the focal length of the imaging system. We can also alter the direction of the shear by rotating the grating. A gradient-based iterative algorithm is used to reconstruct the wavefront from a set of shear interferograms. The results presented in this study demonstrate the first step towards wavefield sensing in the terahertz band without using a reference wave.



## 1. Introduction

Over the last four decades terahertz (THz) radiation has found a variety of applications [1] owing to the combination of two important characteristics. Firstly, it is capable to penetrate many materials, allowing non-destructive testing in many contexts. Secondly, unlike X-rays it is non-ionizing and, therefore, safe for humans [2]. These advantages have fueled the development of THz-devices of many types, including sources and detectors [3], quasi-optical components such as lenses [4] and wave-plates [5]. Accordingly, THz-radiation has found a wide range of applications including biomedical imaging [6], quality control of food and agricultural products [7] and other forms of non-destructive testing [8]. Many of these applications benefit from the capacity of sensing the terahertz electromagnetic wave provided by time-domain spectroscopy (TDS), a technique introduced in the 1980s, which involves the use of ultrafast lasers. The detection of the electromagnetic wave is acquired pixel by pixel and is performed by the cross-correlation between a relatively short (∼ 1 ps) broad-band terahertz electromagnetic transient and a femtosecond optical pulse that either gates a photoconductive detector or probes the birefringence induced in an electrooptic crystal by the THz electric field among other methods [9]. The pixel by pixel acquisition is time consuming and causes a significant limitation, some schemes have been introduced in order to do simultaneous multi-pixel electro-optical sampling which helps to overcome the acquisition time problem, however, they require the use of free-space ultrafast pulses, which limits the applicability of the technique to laboratories with high demands on the required operating temperature stability and laser safety [10, 11].

Since full-field coherent imaging requires less optical components and is fast compared to single point scanning, full-field methods such as digital holography (DH) have the potential to broaden the applicability of THz in many areas, such as biology [12]. DH includes two main

holographic configurations, i.e. in-line as well as off-axis THz digital holography (THz-DH), which are capable to record the amplitude and phase of monochromatic and spatially coherent THz-radiation in a single interference pattern. Both distributions, amplitude and phase, can then be recovered from the interference pattern using spatial [13] or temporal [14] phase-shifting techniques opening the possibility to obtain both 2D and 3D images [15]. Compared to the visible range, THz-DH benefits from wavelength scaling by the larger field of view and lower mechanical stability requirements. In contrast to other THz imaging techniques, THz-DH offers information on the object at various depths since it enables numerical refocusing and layer discrimination from a single hologram. Furthermore, post-processing enables phase contrast imaging with aberration corrections [16], noise suppression [17, 18] and extended depth of focus [19, 20]. In-line THz DH configurations that do not require a reference wave suffer from the overlapping of the twin-image and the zero-order artifacts which reduces the resolution of the reconstruction. Several methods were used to enhance the limited object reconstruction image resolution [21, 22]. To provide spectroscopic information in addition to the amplitude and phase, broadband pulse time-domain holography was proposed [23, 24]. However, the technique offers the measurement of a relatively small area since no large electro-optic crystals are available and this limits its capabilities. On the other hand, off-axis DH schemes offer more freedom when constructing a setup since it is often possible to set large angles at the reference wave [25, 26]. Such a reference wave enables the separation of the twin-image and the zero order. However, the major drawback of off-axis THz-DH is that a reference wave with known characteristics is required. Moreover, the alignment and guidance of the reference wave is critical. Finally, the technique reduces the available space bandwidth product of the camera and thus the the spatial resolution is reduced.

Accordingly, both off-axis DH and time domain based THz-approaches are based either on a superimposeds reference wave field, or a reference pulse for electronic or electrooptic gating. This constitutes an unresolved problem since there are currently no means to analyze a priori unknown THz radiation, for example emitted by antennas, non-linear photonic components, self-luminous emitters or stellar objects or other sources.

Alternatively, single beam methods which are based on THz Hartmann wavefront sensor [27] and phase retrieval (PR) [28] overcome problems arsing from the use of a reference wave. However, wavefront having large slop or sudden changes can not be detected by Hartmann sensor. Thus, test wavefront as well as wavefield with singularities can not be measured. Moreover, the low number of Hartmann mask's holes limits the spatial resolution [24]. On the other hand, for successful phase retrieval diversity of the captured set of intensity patterns is required [29, 30]. Thus smooth wavefields, e.g plane wave, can not be measured.

Common-path shear-interferometry (SI) [31, 32] provides a solution to these limitations, as it uses a reference-free interferometer in which the object wavefield is superimposed with a copy of itself. This approach provides extraordinary flexibility of the setup, reduces the limitations regarding the temporal coherence and increases the stability of the setup compared with DH based approaches. In addition, in contrast to Hartmann sensors and PR, wavefronts with large slops as well as arbitrary wavefields with singularities, e.g. speckles, can be measured.

In this paper we demonstrate the first shear interferometry in the THz-Regime for referenceless wavefield sensing. For this purpose, we use a grating shear interferometer (SI) and designed and fabricated specific optical components for the terahertz band, the most important being a Ronchi phase grating (RPG). We constructed this THz-SI by placing the RPG at the Fourier plane of a $4f$-imaging system. This concept has been used in the visible spectral range [33]. Yet, to the best of our knowledge, this is the first realization of such a system for the THz-regime. In the following sections we will discuss the concept behind the interferometer including the fabrication and characterization of the RPG, the construction of the setup and the proposed approach to recover the wavefront of a spherical wave.

## 2. Grating based shear-interferometer

Figure 1 shows a schematic of the proposed setup of the THz-SI. It consists of a THz source that emits an electromagnetic wave with a wavelength of $\lambda$, a $4f$-arrangement with two identical lenses having the same focal length $f$ and an RPG inserted in the common Fourier plane and a THz camera sensor. The RPG is characterized by its grooves depth $d$ and period $\Delta p$ while the distance between the THz source and the aperture/input plane of the $4f$-setup refers to $z_{ill}$. The first lens performs a Fourier transform of the field generated across the input plane. The field propagates through the common Fourier plane and is modified by the transmittance of the RPG. Subsequently, the second lens performs another Fourier transform of the modulated field onto its back focal plane where a THz camera is located. Without the RPG, the two lenses provide a reversed $1:1$ image of the input plane at the camera. When using an RPG with optimal-depth grooves, 40.5% of light is diffracted into the $+1$ or $-1$ diffraction orders respectively [34] and the rest to the higher odd orders. These orders are separated by the shear $s$ which depends on the wavelength, the focal length of the $4f$ system and the period of the RPG. We refer to this scheme as an RPG-based shear interferometer.

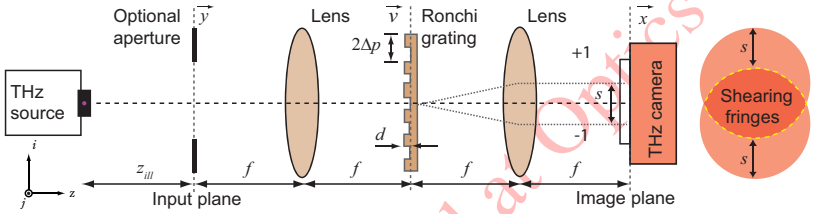


Fig. 1. Schematic of the shear interferometer implemented at 0.28 THz using a $4f$-setup and a Ronchi phase grating as a shear element. $z_{ill}$ is the distance between the THz-source and the input plane where an optional aperture is placed and $f$ is the focal length of the two identical lenses of the $4f$ arrangement. $2\Delta p$ and $d$ are the period and the groove depth of the grating. $+1$ and $-1$ represent the first orders of the grating which are separated by a shear $s$. The vectors $\vec{y}$, $\vec{v}$ and $\vec{x}$ are 2D vectors across the input, Fourier and image planes of the setup, respectively. The scheme to the right illustrates the sheared two copies of the test wavefront generated at the image plane of the camera and shows the region of interest (ROI) where the two copies are overlapping.

Here, the design parameters of the RPG-based SI, such as the focal length of the lenses and the period of the grating, are selected in order to generate the superposition of the $+1$ and $-1$ diffraction orders at the imaging plane where a THz camera is located, as illustrated by the scheme to the right in Fig. 1. It is noted, that the other diffraction orders are filtered out by the subsequent apertures of the second lens and the camera, in analogy to the design of $4f$-system proposed in [35]. In addition, the two beams have the same optical path which relaxes the coherence requirements and ensures the robustness of the setup.

Now we will describe the design parameters of the RPG-based SI. Let us assume that the complex amplitude of the wave field at the aperture plane is $U_{in}(\vec{y})$. Since the configuration represents a linear shift-invariant system, the complex amplitude of the wavefield $U_{img}(\vec{x})$ generated across the camera plane can be written as

$$U_{img}(\vec{x}) = U_{in}(\vec{y}) \otimes \mathcal{F}\{t(\vec{v})\}\left(\frac{\vec{x}}{\lambda f}\right), \tag{1}$$

where, $\vec{y} = -\vec{x}$ are two parallel space vectors at the input and the camera planes, respectively, $\lambda$ is the wavelength of the beam, $\mathcal{F}$ refers to the Fourier transformation, $\vec{v} = (v_i, v_j)$ is a vector at the RPG plane, and $t(\vec{v})$ is the RPG transmittance. If we assume that the grating vector

$\vec{g} = (2\pi/2\Delta p)\vec{e}_i$ with the unit vector $\vec{e}_i$ lying in the grating grid surface gives the direction of its periodicity, $t(\vec{v})$ can be written in the form

$$\begin{aligned} t(\vec{v}) &= \left[\exp\left(\mathrm{i}\frac{\phi}{2}\right)\cdot \mathrm{rect}\left(\frac{1}{\pi}\vec{v}\cdot\vec{g}\right)\otimes\delta\left(v_i+\frac{\Delta p}{2}\right)+\exp\left(-\mathrm{i}\frac{\phi}{2}\right)\cdot\mathrm{rect}\left(\frac{1}{\pi}\vec{v}\cdot\vec{g}\right)\right. \\ &\left.\otimes\delta\left(v_i-\frac{\Delta p}{2}\right)\right]\otimes\frac{1}{2\Delta p}\mathrm{comb}\left(\frac{1}{2\pi}\vec{v}\cdot\vec{g}\right). \end{aligned} \tag{2}$$

Here $\phi$ is the phase introduced by the grooves of depth $d$ of the RPG. It can be estimated as

$$\phi = 2\pi(n_m-1)d/\lambda\,, \tag{3}$$

where $n_m$ is the refractive index of the RPG material. $\mathrm{rect}(\cdots)$, $\delta(\cdots)$ and $\mathrm{comb}(\cdots)$ are the rectangle, Dirac delta and Dirac comb functions, respectively [36]. The Fourier transformation of the transmittance is

$$\mathcal{F}\{t(\vec{v})\}(\vec{\xi}) = \left[\mathrm{sinc}\left(\pi\frac{\vec{g}\cdot\vec{\xi}}{|\vec{g}|^2}\right)\cdot\cos\left(\frac{\phi}{2}+\pi^2\frac{\vec{g}\cdot\vec{\xi}}{|\vec{g}|^2}\right)\right]\cdot\sum_{n=-\infty}^{\infty}\delta\left(\vec{\xi}-\frac{1}{2\pi}n\vec{g}\right), \tag{4}$$

where $n$ is an integer corresponding to the index of the diffraction order and $\vec{\xi} = \vec{x}/\lambda f$ is a vector of spatial frequencies. The last term of Eq. (4) is a comb function that generates the laterally shifted diffraction orders at the camera plane. By setting the arguments of the $\delta$-function of the series equal to zero in the third term of Eq. (4), we obtain that the diffraction orders are separated by $\vec{\xi}_n = (n/2\Delta p)\vec{e}_i$ from the frequency center at $\vec{\xi}_0 = 0$. However, the cosine function term indicates the suppression of the even diffraction orders, i.e. $n = \pm 2, \pm 4, \cdots$. Here, the $\pm 1$ diffraction orders are separated by $\xi_{i,+1} - \xi_{i,-1} = 1/\Delta p$. Using the substitution $\vec{\xi} = \vec{x}/\lambda f$, the magnitude of the shear $s$ can be written as

$$s = |x_{i,+1} - x_{i,-1}| = \frac{\lambda f}{\Delta p}. \tag{5}$$

Consequently, the RPG has to be designed in order to modulate the field across the common Fourier plane such that two laterally shifted copies of the input field centered around the positions of the $+1$ and $-1$ diffraction orders are generated. If these copies overlap, an interference pattern depending on the input wavefield and the shear appears. According to Eq. (1), the intensity of the interference pattern $I(\vec{x})$ will take the form

$$\begin{aligned} I(\vec{x}) = |U_{img}(\vec{x})|^2 &= \left|U_{in}\left(\vec{x}-\frac{\vec{s}}{2}\right)+U_{in}\left(\vec{x}+\frac{\vec{s}}{2}\right)\right|^2 \\ &= I_0(\vec{x})+\mathcal{R}\left\{U_{in}^*\left(\vec{x}-\frac{\vec{s}}{2}\right)U_{in}\left(\vec{x}+\frac{\vec{s}}{2}\right)\right\}, \end{aligned} \tag{6}$$

where, $I_0(\vec{x})$ is the background intensity, $\mathcal{R}\{\cdots\}$ refers to as the real part of a complex number and $*$ refers to the complex conjugate. It is noted, that $\mathcal{R}\{\cdots\}$ represents the interference terms which contain the phase information.

## 3. Wavefront reconstruction using computational shear-interferometry

The main feature of SI is that the measurements represented Eq. (6) can be used to recover finite differences $\Delta\phi(\vec{x})$ of the test wavefront $\phi(\vec{x})$ using spatial or temporal phase-shifting techniques. However, these finite differences must be integrated to reconstruct the wavefront under investigation. In the following section, we present the iterative gradient-based scheme to reconstruct the test wavefront.

Reconstruction of a wavefront from finite differences is an ill-posed inverse problem [37] which is communally solved using optimization theory by minimizing the following objective function [38]

$$L(f) = \sum_{m=1}^{M} \gamma_n(\vec{x}) \|\Delta_m f(\vec{x}) - \Delta_m \phi(\vec{x})\|^2 , \tag{7}$$

to find the wavefront estimate $\tilde{f}$ so that $\tilde{f} = \arg\min_f \{L\}$. The factor $\gamma_n(\vec{x})$ given by $\gamma_n(\vec{x}) = a\,(\vec{x} - \vec{s}/2)\,a\,(\vec{x} + \vec{s}/2)$ is a weighting factor which is inherently obtained from the spatial phase shifting approach. Accordingly, Eq. (7), the sum of the distance squared error (SDS-error) is minimized which yields the least-squares solution to the problem. For this purpose, $M$ shear measurements are required. In Eq. (7), $\|\cdots\|^2 = \sum_{\vec{x}\in R} |\cdots|^2$ and $R$ refers to the the camera's grid. Because of the implemented weighting no direct solution to the problem in analogy to the approach presented in Ref. [37] can be used. In the following, finding the minimum of $L$ which represents the least-squares solution will be achieved by using a gradient-based iterative process for a convex problem [39, 40]. We start with an initial guess $f^{(0)}$ which will be iteratively improved. At the $l^{th}$ iteration, the current estimate $f^{(l)}$ can be written in the form

$$f^{(l)} = f^{(l-1)} - \alpha^{(l-1)} \cdot \nabla L^{(l-1)} . \tag{8}$$

A method to explicitly derive the gradient $\nabla L$ of the proposed objective function is presented in [38]. In Eq.(8), $\alpha^{(l-1)}$ is a scalar parameter defined in each iteration using a non-linear search loop to yield the minimum of $L$.

## 4. Experimental results and discussions

### 4.1. Design, fabrication and characterization of Ronchi grating

As discussed above, the key element of the THz-SI is the RPG. We designed an RPG with a period of $2\Delta p = 6.44$ mm and a groove depth of $d = 1021\,\mu$m, obtained by inserting $\phi = \pi$ in Eq. (3) and optimized for $\lambda = 1.07$ mm corresponding to 280 GHz. Based on Eq.(5), the grating will produce a shear of $s = 23.5$ mm for $f = 142$ mm. We fabricated this structure using mechanical milling on a block of high-density polyethylene (HDPE) with a computer numerical control (CNC) machine. The refractive index of HDPE is $n_m = 1.5238$ at 0.28 THz while its absorption coefficient is $< 0.1$ cm$^{-1}$ as obtained from [41].

Figure 2(a) shows a photo of the RPG fabricated from HDPE and Fig. 2(b) shows the 3D profile determined by a Keyence confocal 3D laser scanning microscope (VK-X3000) with a 10× objective to measure the depth $d$ and the period $2\Delta p$ of the grooves on the fabricated RPG. The depth $d$ and period $2\Delta p_i$ are $0.993 \pm 0.01$ mm and $6.438 \pm 0.084$ mm considering a measurement uncertainty of $3\sigma$ respectively. Theoretically, the normalised diffraction efficiency $\eta_n$ for all the diffraction orders, $n = 0, +/-1, \cdots$, can be calculated from Eq. (4) using

$$\eta_n = |\mathcal{F}\{t(\vec{v})\}(\vec{\xi})|^2 = \left|\mathrm{sinc}\left(\frac{n}{2}\right) \cdot \cos\left(\frac{\phi}{2} + n\frac{\pi}{2}\right)\right|^2 . \tag{9}$$

Notice that this equation provides the diffraction efficiency $\eta_n$ for all the diffraction orders $n$. Optimal grating grooves require a phase modulation of $\pi$ which leads to $\eta_{+1} = 40.5\%$ and $\eta_0 = 0$. Experimentally, we measured $\eta$ using a setup consisting of the THz source, a single lens and the RPG and a camera. The distances between the components were adjusted in order to focus the THz spherical beam on the camera plane, i.e. camrea plane is in the far-field. Thus, the diffraction orders are separated. Figure 2(c) shows the image used to calculated the diffraction efficiency of the RPG. The measured values are $\eta_0 = 2.45\%$ and $\eta_{\pm 1} = 39.54\%$ for the zero and first orders, respectively. It is noticed, that light diffracted into the zero order is smaller than the radiation reflected from a single surface of a lens ($\sim 4\%$) in standard visible interferometers and

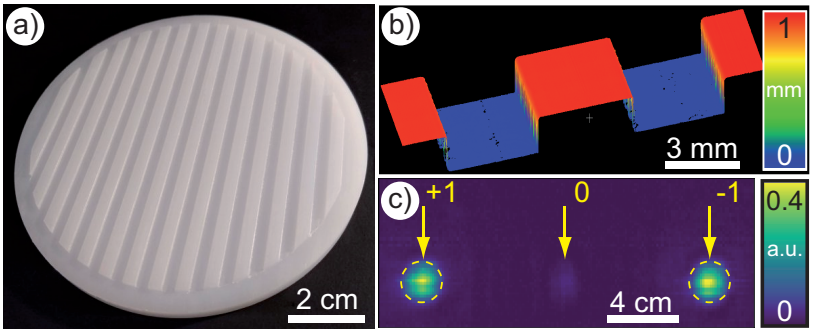


Fig. 2. Fabricated Ronchi phase grating: a) Photo of the grating which is characterized using a confocal microscope. b) Resulting height profile. c) Diffraction efficiencies of the ±1 and the 0 diffraction orders are measured indicating about 40% in the +1 or −1 orders and < 3% in the 0 order. For more details refer to the text.

we expect that this will not significantly affect the main signal of the proposed RPG-based SI. In addition, we want to point out that the circular shape of the focused +1 and −1 orders at the camera plane indicates that there is minimal wavefront distortion caused by the imaging system since the spots have a circular shape.

### *4.2. Experimental setup of the proposed RPG-based SI*

Figure 3 shows the experimental setup based on the scheme shown in Fig. 1. We use an impact ionization avalanche transit time (IMPATT) diode from TeraSense Corp. as THz source, which emitts at 280 GHz ($\lambda = 1.07$ mm). The beam has a Gaussian shape with a power of about 40 mW which is directly measured behind the detachable high gain diagonal horn. The emitting spherical waves propagate through the $4f$-imaging system which we constructed using two identical lenses with $f = 142$ mm at $\lambda = 1.07$ mm. We fabricated the lenses from TOPAS cyclic-olefin-copolymer using 3D printing. [42] The distance between the horn and the input plane of the $4f$-system is $z_{ill} = 150$ mm. A line-array THz camera consisting of 256 pixels, with a pixel pitch of $\Delta p_c = 0.5$ mm was located at the THz image plane. 2D images were formed by scanning the line-array along the horizontal axis using a PI translation stage.

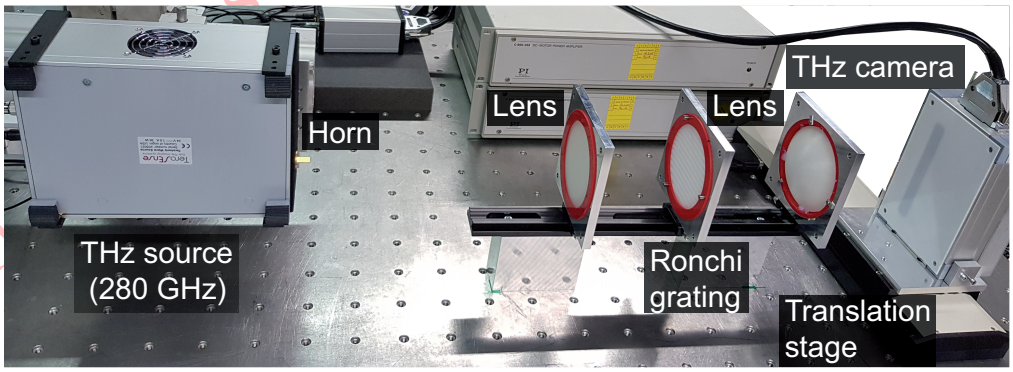


Fig. 3. Photograph of the experimental RPG-based THz SI-setup. The THz source emits a spherical beam at 280 GHz which is shaped to a Gaussian beam by using a detachable high gain diagonal horn. The imaging system consists of two lenses with $f = 142$ mm and a Ronchi grating. The imaged wavefield is recorded using a THz line camera fixed on a translation stage.

### 4.3. Shear interferograms of a spherical wave

We can determine the propagation of a spherical THz beam through the setup in order to calculate the expected interference pattern generated at the camera plane. By using the Fresnel approximation, the spherical wave $U_{in}$ at the input plane of the $4f$-system can be written as

$$U_{in}(\vec{y}) = \frac{a(\vec{y})}{z_{ill}} \cdot \exp\left[ik z_{ill}\left(1 + \frac{|\vec{y}|^2}{2z_{ill}^2}\right)\right] \tag{10}$$

here, $a(\vec{y})$ is the real amplitude of the spherical wave, $k = 2\pi/\lambda$ is the wave number and $z_{ill}$ is the distance between the source and the input plane of the $4f$-system, i.e. radius of curvature. According to Eq. (6) the interference term, in this case, the third term, can be written as

$$U_{in}^{*}\left(\vec{x} - \frac{\vec{s}}{2}\right) U_{in}\left(\vec{x} + \frac{\vec{s}}{2}\right) = B\left(\vec{x}\right) \cdot \exp\left(i\frac{k}{z_{ill}}\vec{s} \cdot \vec{x}\right) \tag{11}$$

with $B(\vec{x}) = a\left(\vec{x} - \vec{s}/2\right) a\left(\vec{x} + \vec{s}/2\right)/z_{ill}^2$. Accordingly, the generated interference pattern is dominated by a linear phase, which appears in the last term of Eq. (11) and depends on the magnitude of the shear $\vec{s}$ and the beam curvature $z_{ill}$.

Figure (4) shows two examples of recorded interferograms of the two shifted spherical waves. These are interference patterns modulated with a spatial carrier frequency of $\vec{\xi}_c = k\vec{s}/2\pi z_{ill} = |\vec{s}|/\lambda z_{ill}$. Accordingly, the shift $\vec{\Delta}_\xi$ of the interference term at the frequency plane in pixels is given by [43]

$$\vec{\Delta}_\xi = \frac{\vec{\xi}_c}{|B_c|} = \frac{\vec{s} N \Delta p_c}{\lambda z_{ill}}\,. \tag{12}$$

Here, $|B_c| = 1/(N\Delta p_c)$ with the number $N$ of the camera pixels in one direction. This knowledge can be used, firstly, to characterize the THz beam at the input plane of the $4f$-setup by determining the radius of beam curvature $z_{ill}$ and, secondly, in order to reconstruct the corresponding phase differences information by applying the spatial carrier frequency method [13].

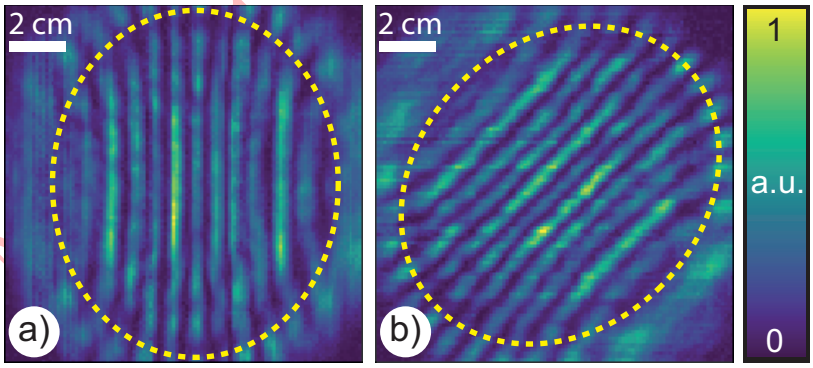


Fig. 4. Two recorded patterns of the test spherical wave obtained for two shears having the same magnitude but different directions, $\vec{s} = (s_i, s_j)$: a) obtained for $s_1 = (23.5, 0)$ mm, i.e. RPG grooves are horizontally aligned and b) by rotating the RPG by 45° to realize a shear of $s_4 = (16.5, 16.5)$ mm. The yellow circles show the overlap area.

In order to determine the shift $\vec{\Delta}_\xi$ with sub-pixel accuracy, the Fourier transform of the interferogram is calculated. Thereafter, the brightest points which correspond to the +1, 0, and −1 diffraction orders are defined. Consequently, an area around the +1 order having the size of

$15 \times 15$ pixels is selected. Values within that area are fitted to a parabolic function. The apex position of the parabolas give the position of the +1 order and the shift $\vec{\Delta}_\xi$ is the relative position of the +1 order to the center. From the interferogram shown in Fig. 4a, the shift is found to be $\Delta_\xi = (18.75, 0)$ pixels. Substituting the values, $N = 256$ pixels, $\Delta p_c = 0.5$ mm, $\lambda = 1.07$ mm, $s = 23.5$ mm, the beam curvature of the spherical wave is $z_{ill} = 149.93$ mm. This agrees with the parameter given for our setup.

The two phase difference maps, obtained after applying the spatial phase shifting approach [44] to the two interferograms, are shown in Fig. 5. For $m$ measurements, the corresponding phase differences $\Delta_m\phi$ resulting after applying the symmetric shears $\vec{s}_m$ can be written as

$$\Delta_m\phi(\vec{x}) = \phi\left(\vec{x} + \frac{\vec{s}_m}{2}\right) - \phi\left(\vec{x} - \frac{\vec{s}_m}{2}\right). \tag{13}$$

These phase difference maps are the input information required to recover the wavefront from the recorded THz interferograms by using computational shear-interferometry (CoSI) [45] which is discussed in more detail in Sec. 3.

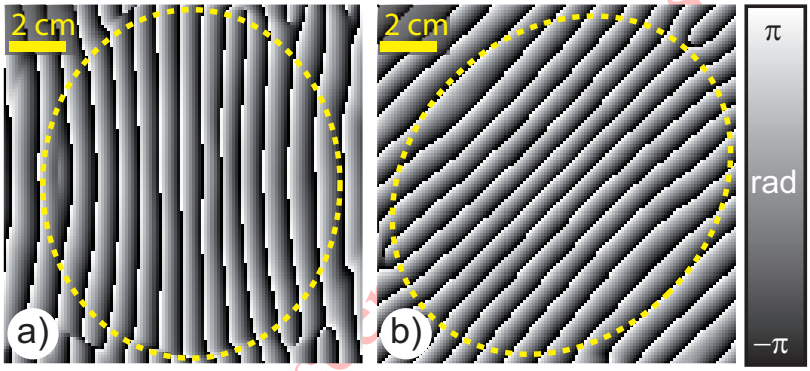


Fig. 5. Recovered spatial phase information from the captured interferograms shown in Fig. 4. The yellow circles indicate the region of interest (ROI) where the two orders, ±1 diffraction orders, are interfering.

In order to experimentally verify this approach, we performed two sets of shear measurements. One for a test wavefront, which we obtained when all setup components were aligned to the optical axis as shown in Fig. 1. For the second set, a wavefront tilt was added to the test wavefront by shifting the THz source laterally from the optical axis of the setup. In each set, seven measurements with shears of the same magnitude but different directions were performed. This was achieved by rotating the RPG at 15° increments starting from 0° and ending with 90°. Accordingly, seven interference patterns including the two patterns shown in Fig. 4 were recorded. Thus, the corresponding seven phase difference maps $\Delta\phi_m$ were reconstructed based on the spatial carrier frequency method as mentioned above. These phase maps were unwrapped by using the PUMA phase unwrapping method [46]. The unwrapped phase maps, obtained for the phase difference maps presented in Fig. 5, are shown in Fig. 6(a,b).

In order to reconstruct the test wavefront from the unwrapped phase maps, we implemented the iterative scheme presented in Eq. (8). As an initial guess the Kronecker delta was used. The iterative process was stopped when the change between two successive iteration fell below certain threshold $\epsilon$. In order to better understand the process, the convergence of the recovered wavefront can be visualized in the animated version of Fig. 7, [see Visualization 1]. Panel a) in the animation shows the progressively improved wavefront recovered from each iteration of Eq. (8). In Fig. 7b, the SDS-error is shown as function of $\alpha$ for each iteration. $\alpha$ is selected to

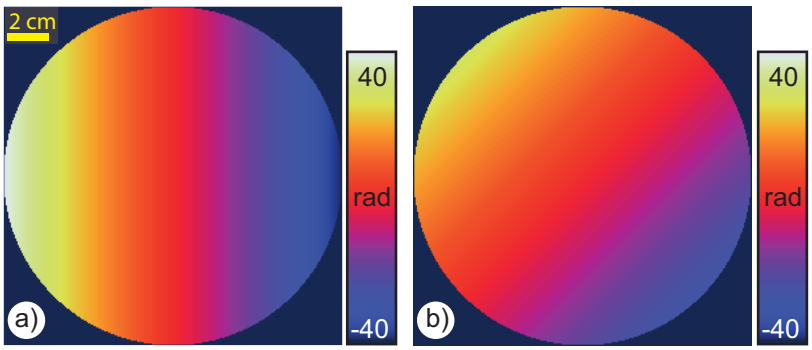


Fig. 6. Examples of unwrapped phase maps used for the reconstruction: a) and b) Two examples of unwrapped phases calculated from the measurements presented in Fig. 5(a,b).

follow the direction of the gradient which minimizes the objective function $L$. In Fig. 7c, the SDS-error is plotted as a function of iterations is presented to monitor the convergence of the iterative scheme.

The solutions of the minimisation are shown in Fig. 8(a,b). For the two measured wavefronts, the stop criteria, i.e. $\epsilon = 0$, is reached at 47 iterations and thus the iterative process reaches its convergence. It is noted that $\alpha$ typically takes values from $6.67 \cdot 10^{-8}$ to $1.4 \cdot 10^{-1}$. What we obtained for the first measurement set is a spherical wavefront. On the other hand, the reconstructed wavefront from the second measurement set is a spherical wavefront modulated with a linear phase ramp which is proportional to the lateral shift of the source and corresponds to a wavefront tilt.

In order to quantitatively evaluate the reconstructed wavefronts shown in Fig. 8(c,d), a Zernike polynomial decomposition was used [47]. Thus, wavefront aberrations, such as tilt and defocus, could be accurately evaluated and hence the radius of curvature of the spherical wave can be determined. The computed Zernike coefficients of the two recovered wavefronts are shown in Fig. 9. One can see the dominant modes include a constant offset phase which represents the 1 mode and the defocus mode, i.e mode 5 ($\mathcal{Z}_5$). Based on the Zernike coefficient of the fifth mode, the beam radius of curvature $z_{ill}$ can be calculated from [48]

$$z_{ill} = \frac{D^2}{4\mathcal{Z}_5}, \tag{14}$$

where $D$ is the radius of the measurement aperture. The computed Zernike coefficients of the fifth mode of both tested wavefronts are equal, $\mathcal{Z}_5 = 6.78\,\text{mm}$. This agrees with our measurement procedure since we shifted only the source laterally and did not change the distance $z_{ill}$. Substituting into Eq. (14) yields a radius of curvature of $z_{ill} = 151.03\,\text{mm}$ with a standard deviation of $\sigma = 0.08\,\text{mm}$ which corresponds to a root mean square wavefront error (RMSE) of $\approx \lambda/12$. In addition, the distorted wavefront shows a tip tilt in the vertical as well as the horizontal axes as expected. This agrees with the effect introduced by laterally shifting the THz source.

Finally, we discuss the limitations of the technique with respect to the properties of the test wavefield, the coherence properties of the illumination, and the imperfection of the grating. Since SI in THz range exhibits all properties of conventional visible SI, arbitrary wavefields having singularities should be measurable in analogy to [45] which should therefore be a subject of future works. Due to the telecentric nature of the $4f$-setup, light incident on the aperture plane requires the same time to travel to the image plane, assuming a flat object. In this case, any effect of the temporal coherence is negligible due to this common path property. However,

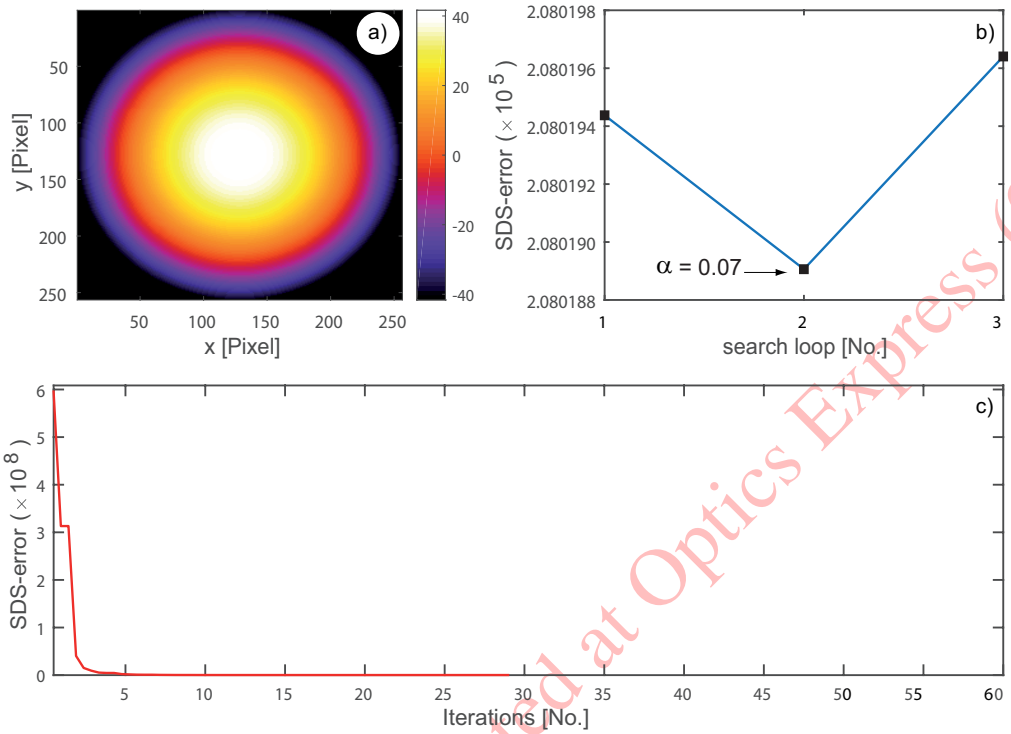


Fig. 7. Convergence of the gradient-based iterative process: a) Reconstructed unwrapped wavefront at 29 iteration. b) Non-linear search loop applied to chose the parameter $\alpha$ which minimise $L$ at the 29 iteration. c) Behaviour of the sum of distance squared error (SDS-error) calculated from each iteration as a function of iterations. The process is visualized in the animation of the Visualization 1.

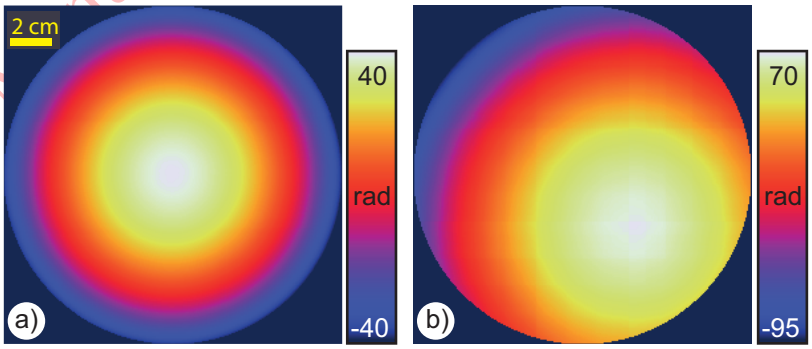


Fig. 8. Experimental results: a) and b) Solutions of the iterative procedure for the test wavefront and its distorted version.

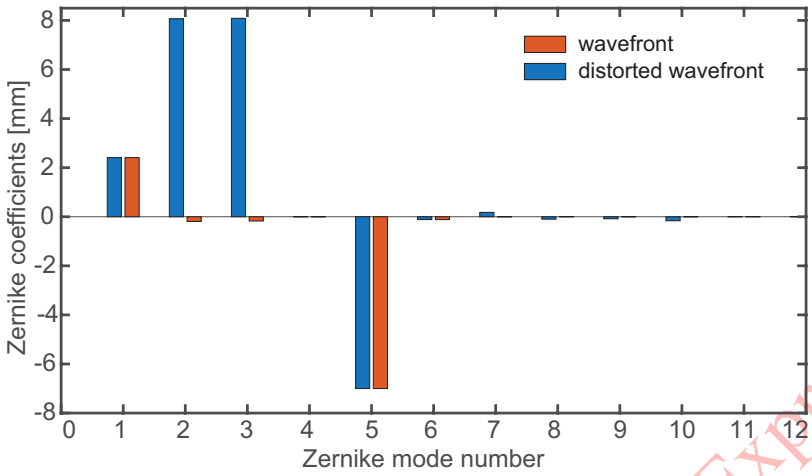


Fig. 9. The plot shows the computed Zernike coefficients of the first 12 Zernike polynomials for the test and the distorted THz wavefronts recovers using the proposed approach and shown in Fig 8(c,d).

for a test object showing large height or thickness variations, the contrast will be reduced if the temporal coherence is less than the object's height or thickness variation. Accordingly, in SI light diffracted from surface points separated by the shear is correlated if the temporal coherency is larger than the surface height or thickness variation. Additionally, spatially separated points are correlated if the shear is selected to be less than the spatial coherence as discussed in [49]. This can be obviously controlled by adjusting the $z_{ill}$ accordingly. However, the most critical parameter which affects the measurement is the gratings grooves depth which should be optimally fabricated as defined by Eq. (3). Any deviation from the optimum value will lead to diffract more light into the even diffraction orders and thus weaken the odd diffraction orders. This of course will significantly disturb the resulting interference pattern. Since the shear is defined from the captured interferograms, the tilt of the grating and/or deviation of the designed grating period are considered within the reconstruction approach.

## 5. Conclusions

In conclusion, we presented a new THz common-path wavefield sensor based on a shear-interferometer. The setup consists of a phase Ronchi grating located across the common plane of a $4f$-imaging system. We fabricated the lenses and grating required for THz radiation at a frequency of 280 GHz. Using confocal microscopy, we characterized the grating in order to determine its groove depth and period. The Ronchi phase grating achieves a diffraction efficiency of the $\pm 1$-orders of 39.5% compared with the 40.5% for the theoretically calculated ideal groove dimensions. Since the wavefield across the input plane of the imaging system is convoluted with the impulse response of the Ronchi phase grating, two laterally shifted copies of the test wavefield are coherently superimposed, generating interference fringes across the overlap zone. The lateral shift, i.e. magnitude of the shear, depends on the focal length of the imaging system, the wavelength of the THz illumination and the period of the grating. In addition, rotating the Ronchi phase grating leads to a change of the shear direction. As a proof-of-concept we have theoretically predicted and experimentally shown interferograms of a spherical wavefield. In addition, we used the spatial carrier frequency method in order to reconstruct the phase differences from each single interferogram. In order to recover the test wavefronts, a set of seven shear measurements was performed. Based on the proposed gradient-based iterative process,

the test wavefront was reconstructed with a root mean square wavefront error of $\lambda/12$. Our results are the first demonstration of full complex wavefield measurements in the THz regime without using a reference wave.

**Funding.** This work is funded by the Deutsche Forschungsgemeinschaft (DFG) within the project "SensATion" (project no. 423266368).

**Acknowledgments.** The authors thank C. Kapitza, R. Klattenhoff and J. Willmann for their support concerning the construction of the setup and the characterization of the Ronchi phase grating and the THz lenses. ECC acknowledges the support of the Alexander von Humboldt Foundation through an Experienced Research Fellowship.

**Disclosures.** The authors declare no conflicts of interest.

**Data Availability.** The data that support the findings of this study are available from the corresponding author upon reasonable request.

## References

1. S. S. Dhillon, M. S. Vitiello, E. H. Linfield, A. G. Davies, M. C. Hoffmann, J. Booske, C. Paoloni, M. Gensch, P. Weightman, G. P. Williams, E. Castro-Camus, D. R. S. Cumming, F. Simoens, I. Escorcia-Carranza, J. Grant, S. Lucyszyn, M. Kuwata-Gonokami, K. Konishi, M. Koch, C. A. Schmuttenmaer, T. L. Cocker, R. Huber, A. G. Markelz, Z. D. Taylor, V. P. Wallace, J. A. Zeitler, J. Sibik, T. M. Korter, B. Ellison, S. Rea, P. Goldsmith, K. B. Cooper, R. Appleby, D. Pardo, P. G. Huggard, V. Krozer, H. Shams, M. Fice, C. Renaud, A. Seeds, A. Stöhr, M. Naftaly, N. Ridler, R. Clarke, J. E. Cunningham, and M. B. Johnston, "The 2017 terahertz science and technology roadmap," J. Phys. D: Appl. Phys. **50**, 043001 (2017).
2. Q. Sun, Y. He, K. Liu, S. Fan, E. P. J. Parrott, and E. Pickwell-MacPherson, "Recent advances in terahertz technology for biomedical applications," Quant. Imaging Medicine Surg. **7**, 345 (2017).
3. E. Castro-Camus and M. Alfaro, "Photoconductive devices for terahertz pulsed spectroscopy: a review," Photonics Res. **4**, A36–A42 (2016).
4. A. Hernandez-Serrano, M. Weidenbach, S. Busch, M. Koch, and E. Castro-Camus, "Fabrication of gradient-refractive-index lenses for terahertz applications by three-dimensional printing," J. Opt. Soc. Am. B **33**, 928–931 (2016).
5. J. Gospodaric, A. Kuzmenko, A. Pimenov, C. Huber, D. Suess, S. Rotter, and A. Pimenov, "3D-printed phase waveplates for THz beam shaping," Appl. Phys. Lett. **112**, 221104 (2018).
6. Q. Sun, Y. He, K. Liu, S. Fan, E. P. Parrott, and E. Pickwell-MacPherson, "Recent advances in terahertz technology for biomedical applications," Quant. imaging medicine surgery **7**, 345 (2017).
7. L. Afsah-Hejri, P. Hajeb, P. Ara, and R. J. Ehsani, "A comprehensive review on food applications of terahertz spectroscopy and imaging," Compr. Rev. Food Sci. Food Saf. **18**, 1563–1621 (2019).
8. I. Amenabar, F. Lopez, and A. Mendikute, "In introductory review to THz non-destructive testing of composite mater," J. Infrared, Millimeter, Terahertz Waves **34**, 152–169 (2013).
9. F. Buccheri, P. Huang, and X.-C. Zhang, "Generation and detection of pulsed terahertz waves in gas: from elongated plasmas to microplasmas," Front. Optoelectronics **11**, 209–244 (2018).
10. M. Brossard, H. Cahyadi, M. Perrin, J. Degert, E. Freysz, T. Yasui, and E. Abraham, "Direct wavefront measurement of terahertz pulses using two-dimensional electro-optic imaging," IEEE Transactions on Terahertz Sci. Technol. **7**, 741–746 (2017).
11. Y. V. Grachev, V. A. Kokliushkin, and N. V. Petrov, "Open-source 3D-printed terahertz pulse time-domain holographic detection module," Appl. Opt. **61**, B307–B313 (2022).
12. Y. Zhang, C. Wang, B. Huai, S. Wang, Y. Zhang, D. Wang, L. Rong, and Y. Zheng, "Continuous-wave THz imaging for biomedical samples," Appl. Sci. **11**, 71 (2021).
13. M. Takeda, H. Ina, and S. Kobayashi, "Fourier-transform method of fringe-pattern analysis for computer-based topography and interferometry," J. Opt. Soc. Am. **72**, 156–160 (1982).
14. I. Yamaguchi and T. Zhang, "Phase-shifting digital holography," Opt. Lett. **22**, 1268–1270 (1997).
15. N. H. Farhat and W. R. Guard, "Millimeter wave holographic imaging of concealed weapons," Proc. IEEE **59**, 1383–1384 (1971).
16. M. Brossard, J.-F. Sauvage, M. Perrin, and E. Abraham, "Terahertz adaptive optics with a deformable mirror," Opt. Lett. **43**, 1594–1597 (2018).
17. M. Kulya, N. V. Petrov, V. Katkovnik, and K. Egiazarian, "Terahertz pulse time-domain holography with balance detection: complex-domain sparse imaging," Appl. Opt. **58**, G61–G70 (2019).
18. M. Kulya, N. V. Petrov, A. Tsypkin, K. Egiazarian, and V. Katkovnik, "Hyperspectral data denoising for terahertz pulse time-domain holography," Opt. Express **27**, 18456–18476 (2019).
19. Z. Sun, C. Li, X. Gao, and G. Fang, "Minimum-entropy-based adaptive focusing algorithm for image reconstruction of terahertz single-frequency holography with improved depth of focus," IEEE Transactions on Geosci. Remote. Sens. **53**, 519–526 (2014).

20. H. Huang, D. Wang, W. Li, L. Rong, Z. D. Taylor, Q. Deng, B. Li, Y. Wang, W. Wu, and S. Panezai, "Continuous-wave terahertz multi-plane in-line digital holography," Opt. Lasers Eng. **94**, 76–81 (2017).
21. Z. Li, L. Li, Y. Qin, G. Li, D. Wang, and X. Zhou, "Resolution and quality enhancement in terahertz in-line holography by sub-pixel sampling with double-distance reconstruction," Opt. Express **24**, 21134–21146 (2016).
22. N. V. Petrov, J.-B. Perraud, A. Chopard, J.-P. Guillet, O. A. Smolyanskaya, and P. Mounaix, "Terahertz phase retrieval imaging in reflection," Opt. Lett. **45**, 4168–4171 (2020).
23. M. S. Kulya, N. S. Balbekin, A. Gorodetsky, S. A. Kozlov, and N. V. Petrov, "Vectorial terahertz pulse time-domain holography for broadband optical wavefront sensing," Proc. SPIE **11279**, 112790D (2020).
24. E. Abraham, H. Cahyadi, M. Brossard, J. Degert, E. Freysz, and T. Yasui, "Development of a wavefront sensor for terahertz pulses," Opt. Express **24**, 5203–5211 (2016).
25. P. Zolliker and E. Hack, "THz holography in reflection using a high resolution microbolometer array," Opt. Express **23**, 10957–10967 (2015).
26. H. Huang, D. Wang, L. Rong, S. Panezai, D. Zhang, P. Qiu, L. Gao, H. Gao, H. Zheng, and Z. Zheng, "Continuous-wave off-axis and in-line terahertz digital holography with phase unwrapping and phase autofocusing," Opt. Commun. **426**, 612–622 (2018).
27. H. Richter, M. Greiner-Bär, N. Deßmann, J. Pfund, M. Wienold, L. Schrottke, R. Hey, H.-T. Grahn, and H.-W. Hübers, "Terahertz wavefront measurement with a hartmann sensor," Appl. Phys. Lett. **101**, 031103 (2012).
28. L. Rong, S. Wang, D. Wang, F. Tan, Y. Zhang, J. Zhao, and Y. Wang, "Transport of intensity equation-based terahertz lensless full-field phase imaging," Opt. Lett. **46**, 5846–5849 (2021).
29. C. Falldorf, M. Agour, C. Von Kopylow, and R. B. Bergmann, "Phase retrieval for optical inspection of technical components," J. Opt. **14**, 065701 (2012).
30. M. Agour, C. Falldorf, and R. B. Bergmann, "Investigation of composite materials using slm-based phase retrieval," Opt. Lett. **38**, 2203–2205 (2013).
31. M. Servin, D. Malacara, and J. Marroquin, "Wave-front recovery from two orthogonal sheared interferograms," Appl. Opt. **35**, 4343–4348 (1996).
32. U. Schnars, C. Falldorf, J. Watson, and W. Jüptner, *Digital Holography and Wavefront Sensing – Principles, techniques and Applications* (Springer, 2015), 2nd ed. Chap. 7.
33. G. Molesini, G. Pedrini, and F. Quercioli, "Laser unequal path interferometer configurations by grating splitting at the Fourier plane," Opt. Eng. **23**, 646–649 (1984).
34. M. S. Heimbeck, P. J. Reardon, J. Callahan, and H. O. Everitt, "Transmissive quasi-optical Ronchi phase grating for terahertz frequencies," Opt. Lett. **35**, 3658–3660 (2010).
35. C. Falldorf, M. Agour, C. von Kopylow, and R. B. Bergmann, "Design of an optical system for phase retrieval based on a spatial light modulator," AIP Conf. Proc. **1236**, 259–264 (2010).
36. J. W. Goodman, *Introduction to Fourier optics* (Roberts and Company Publishers, 2005), 3rd ed.
37. M. Servin, M. Cywiak, and A. Davila, "Lateral shearing interferometry: theoretical limits with practical consequences," Opt. Express **15**, 17805–17818 (2007).
38. C. Falldorf, G. Ehret, M. Schulz, and R. B. Bergmann, "Wave front characterization of gaussian beams using shear interferometry and a weighted reconstructor," in *DGaO Proceedings 2014,* (DGaO, 2014), p. A11.
39. C. Falldorf, C. von Kopylow, and R. B. Bergmann, "Wave field sensing by means of computational shear interferometry," J. Opt. Soc. Am. A **30**, 1905–1912 (2013).
40. M. Agour, C. Falldorf, and R. B. Bergmann, "Shape measurements of microscopic objects using computational shear interferometry," Proc. SPIE **9718**, 321–328 (2016).
41. E. Castro-Camus, M. Koch, and A. I. Hernandez-Serrano, "Additive manufacture of photonic components for the terahertz band," J. Appl. Phys. **127**, 210901 (2020).
42. S. F. Busch, M. Weidenbach, J. C. Balzer, and M. Koch, "THz optics 3D printed with topas," J. Infrared, Millimeter, Terahertz Waves **37**, 303–307 (2016).
43. S. Leveque, C. Falldorf, R. Klattenhoff, and A. Cheffot, "Day-time local phasing of neighbouring segments of the E-ELT primary mirror, based simultaneous multi-$\lambda$ shearing interferometry," Proc. SPIE **9912**, 1379–1390 (2016).
44. T. Sokkar, K. El-Farahaty, M. El-Bakary, E. Omar, M. Agour, and A. Hamza, "Adaptive spatial carrier frequency method for fast monitoring optical properties of fibres," Appl. Phys. B **122**, 138 (2016).
45. C. Falldorf, M. Agour, and R. B. Bergmann, "Digital holography and quantitative phase contrast imaging using computational shear interferometry," Opt. Eng. **54**, 024110 (2015).
46. J. M. Bioucas-Dias and G. Valadao, "Phase unwrapping via graph cuts," IEEE Transactions on Image Process. **16**, 698–709 (2007).
47. M. Born and E. Wolf, *Principles of optics: electromagnetic theory of propagation, interference and diffraction of light* (Cambridge University Press, 1999), 7th ed.
48. T. Binkele, D. Hilbig, T. Henning, and F. Fleischmann, "Determination of the paraxial focal length using Zernike polynomials over different apertures," Proc. SPIE **10110**, 60–69 (2017).
49. C. Falldorf, M. Agour, and R. B. Bergmann, "Advanced wave field sensing using computational shear interferometry," Proc. SPIE **9204**, 92040C (2014).